arXiv:1701.02665v1 [physics.geo-ph] 10 Jan 2017

Revisiting slope influence in turbulent bedload transport: consequences for vertical flow structure and transport rate scaling

Raphael Maurin[1]†‡, Julien Chauchat[2,3] and Philippe Frey[1]

[1]Univ. Grenoble Alpes, Irstea, UR ETGR, 2 rue de la Papeterie-BP 76, F-38402 St-Martin-d'Hères, France

[2]CNRS, UMR 5519, LEGI, F-38000 Grenoble, France

[3]Univ. Grenoble Alpes, LEGI, F-38000 Grenoble, France

(Received xx; revised xx; accepted xx)

Gravity-driven turbulent bedload transport has been extensively studied over the past century with regard to its importance for earth surface processes such as natural riverbed morphological evolution. In the present contribution, the influence of the channel inclination angle on gravity-driven turbulent bedload transport is studied in an idealised framework considering steady and uniform flow conditions. Discussing the origin of the buoyancy force, it is shown that a misconception has led to erroneous results of the slope influence on the critical Shields number corresponding to the onset of motion. Analyzing the phenomenon further in a two-phase continuous framework, the channel inclination angle is shown to not only influence the fluid bed shear stress and the resistance of the granular bed, but also the fluid flow inside the granular bed. These coupled mechanisms affect both the vertical structure of the granular flow and the transport rate scaling law. This cannot be accounted for in the classical sediment transport modelling approach relating the dimensionless sediment transport rate to the Shields number, i.e. the dimensionless fluid bed shear stress taken at the top of the granular bed. Based on an analytical development and using dimensional arguments, a new definition of the Shields number is proposed, including a critical slope that corresponds to the transition between bedload transport and debris flows. The proposed definition is tested against coupled fluid-discrete element method numerical simulations of idealised gravity-driven turbulent bedload transport, for a wide range of Shields numbers, density ratios and channel inclination angles. More than one hundred simulations have been performed and all the data is shown to collapse on a master curve when rescaled by the new Shields number, demonstrating the relevancy of the proposed scaling law. The analysis shows that the channel inclination angle not only influences the critical Shields number, but also affects the entire sediment transport formula through a dependency of the Shields number on the channel inclination angle. The vertical structure of the granular flow is analysed to illustrate the influence of both the channel inclination angle and the Shields number on the depth profiles, allowing us to identify the underlying mechanisms driving the granular depth profile evolution. Lastly, in light of the proposed analysis, the pressure-driven configuration is discussed with respect to the gravity-driven case, evidencing a difference in the channel inclination angle dependency, which underlines the necessity to distinguish these two cases when accounting for the slope influence in turbulent bedload transport.

† Email address for correspondence: raphael.maurin@imft.fr

‡ Present address: Université de Toulouse, INPT, UPS, IMFT (Institut de Mécanique des Fluides de Toulouse), Allée Camille Soula, F-31400 Toulouse, France

This contribution allows us to clarify the role of the slope in turbulent bedload transport and predicts a consistent modification of the Shields number allowing to theoretically make the link between bedload transport and debris flow.

1. Introduction

Considering a granular bed submitted to a fluid flow, three regimes of sediment transport can be defined as a function of the particle to fluid density ratio, ρ^p/ρ^f, and of the suspension number, $S^* = w_s/u^*$- comparing the particle settling velocity w_s and the turbulent bed friction velocity u^*- : suspended load ($S^* < 1$), bedload ($S^* > 1$, $\rho^p/\rho^f \sim 1$) and aeolian saltation ($S^* > 1$, $\rho^p/\rho^f >> 1$).
Turbulent bedload transport ($Re = \rho^f h\ U/\eta^f >> 1$, with η^f the dynamical fluid viscosity, and U the mean fluid velocity in the water depth h) is of major importance for prediction of riverbed evolution and coastal processes, which represents an important issue for public safety, management of water resources, and environmental sustainability. In this framework, the key parameter to predict is the dimensionless sediment transport rate, so-called Einstein's number (Einstein 1942), $Q_s^* = Q_s/\sqrt{(\rho^p - \rho^f)gd^3}$, where Q_s is the volumetric sediment transport rate per unit width, g is the acceleration of gravity, and d the particles diameter. It is classically related to the dimensionless fluid bed shear stress, denoted as the Shields number (Shields 1936), $\theta^* = \tau_b/(\rho^p - \rho^f)gd$, where τ_b is the fluid bed shear stress. Due to the inherent complexity of granular media behavior and turbulent fluid flows, turbulent bedload transport understanding remains limited despite a century of modern research on the subject (Gilbert 1914; Bagnold 1956). This is illustrated by the poor prediction provided by the classical formulas linking Einstein and Shields numbers - such as Meyer-Peter & Müller (1948) formula -, leading to sediment transport rate up to two orders of magnitude different from what is observed in the field (Recking *et al.* 2013). One key aspect of the observed data dispersion might be related to the influence of the channel inclination angle on the sediment transport rate. Accordingly, the present paper focuses on the analysis of the slope influence in turbulent bedload transport.

Most applications of turbulent bedload transport involves the presence of a slope, for example in the case of a beach in coastal sediment transport, a river or a mountain stream. The slope inclination angle is expected to affect the sediment transport rate through a modification of the particles mobility. This is classically accounted for by considering a force balance on a single grain at the top of the granular bed close to the onset of motion (Fredsøe & Deigaard 1992; Andreotti *et al.* 2013). In the zero-slope case (see figure 1), the force balance at the onset of motion reduces to an equality between the streamwise drag force induced by the fluid flow, f_D, and the resistive friction force on the granular layer below. The latter can be expressed as a granular friction coefficient (μ_s) multiplied by the buoyant weight representing the vertical force applied on the grain. Then, the force balance reads:

$$\frac{\pi}{8}\rho^f d^2 C_D u_*^2 - \mu_s \left(\rho^p g\ \frac{\pi}{6} d^3 - f_z^b\right) = 0, \tag{1.1}$$

with C_D is the drag coefficient, $\mathbf{f}^b$ is the buoyancy force and u_* is the velocity scale at the granular bed assimilated to the fluid bed friction velocity. From this balance, by expressing the buoyancy force the critical Shields number can be written as:

$$\theta_c^0 = \frac{\rho^f u_*^2}{(\rho^p - \rho^f)gd} = \frac{4\mu_s}{3C_D}. \tag{1.2}$$

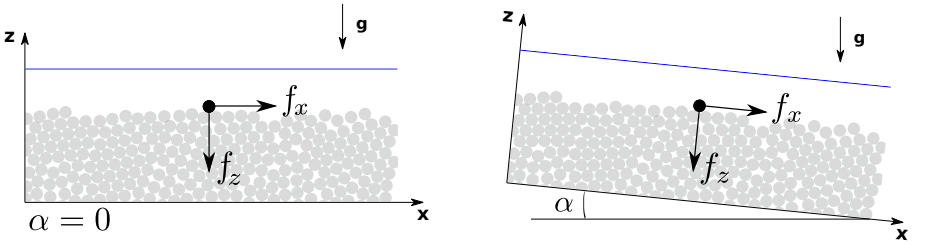

FIGURE 1. Schematic slope influence on a particle at the top of the granular bed at rest.

In the presence of a slope inclination angle, α, (see figure 1) two additional positive terms appear in the force balance due to the projection of the particle weight and buoyancy force along the streamwise axis:

$$\frac{\pi}{8}\rho^f d^2 C_D u_*^2 - \mu_s \left(\rho^p g \cos\alpha \frac{\pi}{6} d^3 - f_z^b\right) + \rho^p g \sin\alpha \, \frac{\pi}{6} d^3 + f_x^b = 0, \tag{1.3}$$

while the friction force is reduced due to the projection of the particle weight along the vertical axis. Taking the buoyancy force as $\mathbf{f}^b = -\rho^f \frac{\pi}{6} d^3 \mathbf{g}$, leads to the following reduction of the critical Shields number with increasing slope:

$$\theta_c(\alpha) = \theta_c^0 \cos\alpha \left[1 - \frac{\tan\alpha}{\mu_s}\right]. \tag{1.4}$$

This expression of the modification of the critical Shields number has been first formulated by Fernandez Luque & Van Beek (1976) considering a moment balance instead of a force balance, resulting in the expression of μ_s as the tangent of the pocket angle formed by the particle and its neighbours. Performing turbulent bedload transport experiments in an inclined rectangular pressure-driven closed conduct, with variation of particle diameter ($d \in [0.9, 3.3]mm$), density ratio $\rho^p/\rho^f \in [1.34, 4.5]$ and channel inclination angle ($\alpha \in [0, 22]^\circ$), Fernandez Luque & Van Beek (1976) found a relatively good agreement between the theoretical prediction and experimental results providing a fit of the pocket angle, which appeared unexpectedly large. Following this pioneering work, Chiew & Parker (1994) reproduced a similar approach, deriving equation (1.4) from a force balance associating μ_s to the granular medium repose angle, and comparing the prediction to experimental data in pipe flows. Varying the particle mean diameter $d \in [0.5, 3]mm$, the repose angle $\Phi \in [33, 38]^\circ$, and the channel inclination angle $\alpha \in [0, 31]^\circ$, they showed that the critical Shields number follows the prediction of equation (1.4) for downward slopes. This work has been further generalized by Dey (2003) to the combined effect of transverse and longitudinal slopes, validating the analysis with experiments in pipe flows.
This type of approach is widespread in turbulent sediment transport and can be found in classical textbooks of sediment transport (Fredsøe & Deigaard 1992) and granular media (Andreotti *et al.* 2013), as well as in the aeolian saltation community (Iversen & Rasmussen 1994, 1999). It has been applied in turbulent bedload transport to experiments and field transport rate predictions (see e.g. Li & Cheng (1999); Wilcock & Crowe (2003); Karmaker & Dutta (2016)).

In the meantime, the slope effect has been studied experimentally in gravity-driven turbulent bedload transport. Considering a large range of slopes, Smart & Jaeggi (1983); Smart (1984) and later Rickenmann (1991, 2001) have determined empirical relationships between the dimensionless sediment transport rate and a modified Shields number. The

latter, classically evaluated from the water-depth h, was determined from the so-called mixture depth h_m including both the water depth h and the thickness of the granular layer in motion δ. While this important difference does not enable a direct comparison as the mobile bed layer thickness (δ) scales with the classical Shields number (Sumer *et al.* 1996; Hsu *et al.* 2004), it is worth noting that these analyses include not only a modification of the critical Shields number by the slope, but also a modification of the Shields number itself and of the law linking the dimensionless sediment transport rate to the Shields number. A similar modification of the sediment transport formula has been proposed by Cheng & Chen (2014), replacing the gravity contribution by a slope-modified gravity in both the Shields and Einstein numbers formulation, and considering the classical Meyer-Peter & Müller (1948) formula. The obtained formula fits the existing experimental data better than the classical corrections (Cheng & Chen 2014), but lacks a solid theoretical justification. Lastly, it is interesting to note that Damgaard *et al.* (1997) also proposed an empirical correction of the transport formula based on experimental data in closed conduct.

The literature review underlines two different trends that seem to be associated with pressure-driven and gravity-driven configurations in turbulent bedload transport. On one hand, gravity-driven experiments exhibit a modification of the transport formula as a function of the slope. On the other hand, the variation of the critical Shields number with the slope seems to be well predicted from a force/moment balance on a single particle in pressure-driven configurations. However, there is a priori no theoretical justification why a variation of the slope should only affect the critical Shields number and the study of Damgaard *et al.* (1997) at moderate Shields numbers suggests a behavior similar to the gravity-driven configuration. This lack of characterization together with the absence of clear theoretical bases in the literature suggests the need for further analysis.

In the present contribution, we attempt to give a better understanding of the slope influence on turbulent bedload transport by adopting an idealized and theoretical point of view. Focusing on gravity-driven turbulent bedload transport under steady uniform flow conditions, we discuss the bases of the critical Shields number derivation and analyze the granular entrainment mechanisms in the framework of the two-phase continuous equations (section 2). This allows us to characterize the influence of the slope on the vertical flow structure and propose a re-scaling of the Shields number to account for the slope influence on the sediment transport rate. The proposed scaling is tested against fluid-discrete element method simulations (section 3) and the theoretical results are discussed more generally in the light of the numerical results, considering in particular the vertical flow structure and the difference between gravity-driven and pressure-driven configurations (section 4).

2. Theoretical analysis

2.1. *Discussion on the classical critical Shields number derivation*

The classical derivation of the critical Shields number reproduced in the introduction relies on the following expression of the buoyancy force applied on a particle:

$$\mathbf{f}^b = -\rho^f \frac{\pi}{6} d^3 \mathbf{g}. \tag{2.1}$$

While this expression is classically used, it does not apply a priori to all the different configurations explored in fluid-particle flow, as stressed out by Christensen (1995).

The buoyancy force is defined as the force a fluid element would undergo if it was occupying the position of the particle (Maxey & Riley 1983). It can be derived explicitely in the Stokes flow case and leads to the following formulation (Maxey & Riley 1983):

$$\mathbf{f}^b = -\frac{\pi}{6} d^3 \ \nabla \sigma_u^f, \tag{2.2}$$

where σ_u^f is the undisturbed fluid stress tensor, i.e. the fluid stress tensor based on the fluid velocity field undisturbed by the presence of the particles. This formulation is used in Jackson (2000) at the level of the continuous medium, including the Reynolds stresses contribution (R^f) inside the fluid stress tensor. However, the formulation of the buoyancy force should not a priori include the contribution from the Reynolds stresses considering that they are associated with advection and related to the time averaging of the fluid velocity fluctuations. Focusing on a single particle in a turbulent Newtonian fluid flow, it experiences a buoyancy force depending on the average fluid velocity field but independent from the fluctuations with time. Indeed, the expression of the buoyancy is linear with the second spatial derivative of the fluid velocity for a Newtonian fluid,

$$\mathbf{f}^b = -\frac{\pi}{6} d^3 \ \eta^f \ \nabla[\nabla \mathbf{u}^\mathbf{f} + (\nabla \mathbf{u}^\mathbf{f})^T], \tag{2.3}$$

so that the time-averaging of the buoyancy force reduces to the contribution from the average fluid velocity field. From this considerations, the expression of the buoyancy force should follow the equation (2.2) in all the different fluid flow regimes (Lhuillier 2011).

As a consequence, the above-mentionned derivation is not valid in uniform gravity-driven turbulent bedload transport as the undisturbed fluid equation, $0 = -\nabla R^f - \nabla \sigma_u^f + \rho^f \mathbf{g}$, together with the regular expression of the buoyancy force (eq. 2.2), does not allow to write the buoyancy force as equation (2.1).
Expressing the buoyancy directly from equation (2.2), it follows $f_z^b = \pi d^3/6 \rho^f g \cos\alpha$ and $f_x^b = -\pi d^3/6 \ \partial_z \sigma_{xz}^f$, by using the hydrostatic characteristics of the fluid along z. Considering that the viscous shear stress contribution is negligible in turbulent bedload transport $\partial_z \tau_{xz}^f \simeq 0$ (Revil-Baudard & Chauchat 2013; Maurin *et al.* 2016), the force balance performed on a particle lying on the granular bed at the onset of motion (eq. 1.3) reads:

$$\frac{\pi}{8} \rho^f d^2 C_D u_*^2 - \mu_s (\rho^p - \rho^f) g \cos\alpha \ \frac{\pi}{6} d^3 + \rho^p g \sin\alpha \ \frac{\pi}{6} d^3 = 0, \tag{2.4}$$

where only the particle weight projection along the streamwise axis is non-negligible. This leads to the following modification of the critical Shields number due to the slope effect:

$$\theta_c(\alpha) = \theta_c^0 \cos\alpha \left[1 - \frac{\tan\alpha}{\mu_s} \frac{1}{1 - \rho^f/\rho^p}\right], \tag{2.5}$$

where the density ratio ρ^p/ρ^f modifies the classical slope effect characterized by equation (1.4). This difference is of importance for underwater bedload transport, where the density ratio is typically of order one ($\rho^p \gtrsim \rho^f$).

Adopting the regular expression for the buoyancy force also affects the derivation of the slope influence on the critical Shields number in the pressure-driven configuration. In this case, the streamwise component of the buoyancy force is completed by the term

due to the presence of a pressure gradient:

$$\frac{\pi}{8}\rho^f d^2 C_D u_*^2 - \mu_s(\rho^p - \rho^f)g\cos\alpha\ \frac{\pi}{6}d^3 + \rho^p g\sin\alpha\ \frac{\pi}{6}d^3 - \frac{\partial P^f}{\partial x} = 0, \tag{2.6}$$

which does not enable to recover the classical modification of the critical Shields number derived in introduction (eq. 1.4). The latter equation remains only valid in the case where the fluid mass column stays at a constant level perpendicular to the gravity, i.e. for underwater avalanches or coastal sediment transport.

2.2. *Vertical granular flow structure and entrainment mechanisms*

Instead of focusing on the critical Shields number modification in a discrete particle framework, we adopt a more general approach based on the continuous two-phase flow framework to analyze the slope influence from the onset of motion up to intense turbulent bedload transport. In order to better understand the vertical structure of the granular flow and the local mechanisms at play, let us express the shear to normal granular stress ratio as a function of the depth $\tau^p_{xz}(z)/P^p(z)$. The yield criterion $\tau^p_{xz}/P^p > \mu_s$ is characteristic of the onset of granular flow, so that the positive contributions to the shear to normal stress ratio at a given height z reflects the local entrainment mechanism of the granular medium.

The two-phase volume-averaged equations read for steady uniform flows (Jackson 2000; Revil-Baudard & Chauchat 2013):

$$0 = \frac{\partial \tau^f_{xz}}{\partial z} + \frac{\partial R^f_{xz}}{\partial z} + \rho^f(1-\phi)g\sin\alpha - n\left\langle f^p_{f\,x}\right\rangle^p, \tag{2.7}$$

$$0 = \frac{\partial \tau^p_{xz}}{\partial z} + \rho^p\phi g\sin\alpha + n\left\langle f^p_{f\,x}\right\rangle^p, \tag{2.8}$$

$$0 = -\frac{\partial P^f}{\partial z} + \rho^f(1-\phi)g\cos\alpha - n\left\langle f^p_{f\,z}\right\rangle^p, \tag{2.9}$$

$$0 = -\frac{\partial P^p}{\partial z} + \rho^p\phi g\cos\alpha + n\left\langle f^p_{f\,z}\right\rangle^p, \tag{2.10}$$

Where $\sigma^f_{ij} = -P^f\delta_{ij} + \tau^f_{ij}$ is the effective fluid stress tensor, $\sigma^p_{ij} = -P^p\delta_{ij} + \tau^p_{ij}$ is the granular stress tensor, R^f_{ij} is the Reynolds stress tensor, ϕ and ϵ are the solid and fluid volume fraction respectively, and $n\left\langle \mathbf{f^P_f}\right\rangle^p$ is the fluid-solid momentum transfer.
Integrating these equations between a position $z < h_p$ in the moving granular layer and h_p, the top of it, allows us to simplify the equations and to express the shear to normal stress ratio as a function of the vertical position z. Focusing on the granular equations (2.8) and (2.10), the granular stress tensor is zero at h_p and the integrated streamwise component of the granular momentum balance leads to:

$$\tau^p_{xz}(z) = \rho^p g\sin\alpha\int_z^{h_p}\phi(\zeta)d\zeta + \int_z^{h_p} n\left\langle f^p_{f\,x}\right\rangle^p(\zeta)d\zeta. \tag{2.11}$$

Assuming that the fluid wall-normal pressure is hydrostatic, the fluid-particle interaction term $n\left\langle f^p_{f\,z}\right\rangle^p$ can be expressed from equation 2.9. Replacing it in equation (2.10), we obtain:

$$P^p(z) = g\cos\alpha(\rho^p - \rho^f)\int_z^{h_p}\phi(\zeta)d\zeta. \tag{2.12}$$

Lastly, the fluid streamwise momentum balance (eq. 2.7) can be integrated between z and h_p in order to express the last term on the right hand side of equation (2.11):

$$0 = \tau^f_{xz}(h_p) - \tau^f_{xz}(z) + R^f_{xz}(h_p) - R^f_{xz}(z) + \rho^f g \sin\alpha \int_z^{h_p} [1-\phi(\zeta)]d\zeta - \int_z^{h_p} n \left\langle f^p_{f\,x} \right\rangle^p (\zeta) d\zeta. \tag{2.13}$$

It has been shown previously in turbulent bedload transport and sheet-flow simulations that the effective viscous shear stress tensor is negligible throughout the depth with respect to the Reynolds stresses in the upper part and to the slope contribution inside the bed (Revil-Baudard & Chauchat 2013; Maurin *et al.* 2016). Furthermore, the Reynolds stresses are fully damped in the granular bed, and we assume that their contribution is negligible in the moving granular layer $R^f_{xz}(z) \sim 0$. Defining the fluid bed shear stress from the maximum of the turbulent shear stress and considering that the latter is located at the top of the granular layer (Revil-Baudard & Chauchat 2013; Maurin *et al.* 2016), $\tau_b = R^f_{xz}(h_p)$, equation (2.14) reads:

$$\int_z^{h_p} n \left\langle f^p_{f\,x} \right\rangle^p (\zeta) d\zeta = \tau_b + \rho^f g \sin\alpha \int_z^{h_p} [1-\phi(\zeta)]d\zeta. \tag{2.14}$$

Combining equations (2.11), (2.12) and (2.14), and defining the average solid volume fraction between z and h_p, $\bar{\phi}_z$ as:

$$\bar{\phi}_z (h_p - z) = \int_z^{h_p} \phi(\zeta) d\zeta, \tag{2.15}$$

the shear to normal stress ratio $\tau^p_{xz}(z)/\tau^p_{zz}(z)$ can be expressed as:

$$\frac{\tau^p_{xz}(z)}{\tau^p_{zz}(z)} = \frac{\rho^p}{\rho^p - \rho^f}\tan\alpha + \frac{\tau_b}{g\cos\alpha(\rho^p-\rho^f)\bar{\phi}_z(h_p-z)} + \frac{\rho^f}{\rho^p-\rho^f}\frac{1-\bar{\phi}_z}{\bar{\phi}_z}\tan\alpha, \tag{2.16}$$

Three contributions to the granular phase shear to normal stress ratio can be identified. The first term on the right hand side of equation (2.16) is constant within the depth, and represents the slope effect on the granular phase. It is analogous to the classical configuration of a dry granular medium on an inclined plane, where the shear to normal stress ratio is constant within the depth and equal to the tangent of the inclination angle α (Andreotti *et al.* 2013). In bedload transport, the presence of a buoyancy force along the vertical axis leads to a modification of this term by the density ratio. The two last terms on the right hand side correspond to the fluid contribution on the granular phase, which has been splitted into two contributions coming from the fluid flow above the bed and the fluid flow inside the granular layer respectively. The Shields number can be identified in the former and the term reduces to:

$$\frac{\tau_b}{g\cos\alpha(\rho^p-\rho^f)\bar{\phi}_z(h_p-z)} = \frac{\theta^*}{\bar{\phi}_z}\frac{d}{h_p-z}. \tag{2.17}$$

This represents the contribution from the fluid bed shear stress to the entrainment of particles. Its surface nature is characterized by a decrease of the contribution inside the granular bed as z decreases. It is accounted for in bedload transport studies, by assuming that the Shields number is representative of the total imposed fluid bed shear stress. However, the contribution from the fluid flow inside the granular layer, corresponding to the third term on the right hand side of equation (2.16), is usually neglected while it is seen to be of importance when increasing the slope angle. This contribution depends on the slope and characterizes the effect of the slope on the fluid flow inside the granular

layer. The latter affects the granular phase through the fluid-particle interaction, and in consequence depends also on the specific density. In addition, the different dependence on the vertical position z of the two fluid terms implies that a modification of the slope at given Shields number and specific density would induce a change in the vertical repartition of the shear to normal stress ratio, and therefore on the vertical structure of the granular flow. This could explain why the velocity and solid volume fraction profiles are not self-similar in gravity-driven bedload transport (Armanini *et al.* 2005; Larcher *et al.* 2007; Capart & Fraccarollo 2011; Frey 2014; Maurin 2015; Maurin *et al.* 2015).

In order to get more insight into the physical meaning of the fluid flow contribution inside the granular bed, let us consider the simple case of a gravity-driven fluid flow through a quasi-static porous granular bed. The Shields number contribution is negligible in this configuration and the granular bed is at rest so that the average solid volume fraction is equal to the maximum packing fraction $\bar{\phi}_z = \phi^{max}$, leading to a shear to normal stress ratio independent from the vertical position z:

$$\frac{\tau^p_{xz}(z)}{P^p(z)} = \frac{\rho^p}{\rho^p - \rho^f}\tan\alpha + \frac{\rho^f}{\rho^p - \rho^f}\frac{1-\phi^{max}}{\phi^{max}}\tan\alpha$$
$$= \frac{\tan\alpha}{\rho^p/\rho^f - 1}\left[\frac{\rho^p}{\rho^f} + \frac{1-\phi^{max}}{\phi^{max}}\right]. \quad (2.18)$$

As a consequence, there exists a critical angle above which the entire granular layer will be entrained independently from its thickness. This avalanche angle α_0 corresponds to the configuration for which the shear to normal stress ratio exceeds the static friction coefficient of the granular medium μ_s:

$$\tan\alpha_0 = \frac{\mu_s}{1 + [(\rho^p/\rho^f - 1)\phi^{max}]^{-1}}. \quad (2.19)$$

This corresponds to the critical angle for the onset of debris flow as derived by Takahashi (1978), and is well-known in the debris flow community (Takahashi 2007). The derivation presented here makes the link between debris flows and gravity-driven turbulent bedload transport, and evidences the importance of the slope influence through the fluid flow inside the granular layer when considering steep slope configurations. In addition, it shows that the expression of the critical angle of debris flow α_0 is characteristic of the slope influence on the granular phase through both its direct impact and the fluid-induced contribution in gravity-driven bedload transport, two mechanisms that depends on the specific density $\rho^p/\rho^f - 1$.

2.3. *Sediment transport rate scaling*

Taking advantage of the developed analysis, we look for a scaling law of the sediment transport rate accounting for the slope effect. Following Bagnold (1956), the sediment transport rate per unit width Q_s can be expressed as a function of the solid volume fraction ϕ and the average particle velocity $< v_x >^s$ profiles:

$$Q_s = \int_0^\infty \phi(z) < v_x >^s (z)dz = \int_{h_c}^{h_p} \phi(z) < v_x >^s (z)dz = \overline{\phi < v_x >^s}\,\delta. \quad (2.20)$$

where h_c is the lower bound of the mobile granular layer, $\delta = h_p - h_c$ is the mobile granular layer thickness, and the $\bar{\bullet}$ denotes the average over z along the mobile granular layer thickness. Considering $z = h_c$ in equation (2.16), the mobile layer thickness can be

expressed as:

$$\frac{\delta}{d} = \frac{\theta^*}{\bar{\phi}\left[\mu_s - \left(1 + [\bar{\phi}(\rho^p/\rho^f - 1)]^{-1}\right)\tan\alpha\right]} \simeq \frac{\theta^*}{\phi^{max}\mu_s\left[1 - \tan\alpha/\tan\alpha_0\right]}. \tag{2.21}$$

where equation (2.19) has been used and it has been assumed that $\bar{\phi} \simeq \phi^{max}$ as the average solid volume fraction $\bar{\phi}$ is only weakly varying in the problem.

The term $\overline{\phi < v_x >^s}$ has the dimension of a velocity, i.e. the square root of the product of an acceleration and a length scale. In the problem, the only acceleration scale is the buoyant reduced gravity $\tilde{g} = (\rho^p/\rho^f - 1)g$ (Duran *et al.* 2012), and we have seen that the relevant length scale is the mobile granular layer thickness. Thus, the volume flux shoud scale as:

$$\overline{\phi < v_x >^s} \sim \sqrt{(\rho^p/\rho^f - 1)g\delta}. \tag{2.22}$$

Compiling equations (2.20), (2.21) and (2.22), the scaling law of the dimensionless sediment transport rate Q_s^* can be written as:

$$Q_s^* = \frac{Q_s}{\sqrt{(\rho^p/\rho^f - 1)gd^3}} \sim \frac{\sqrt{(\rho^p/\rho^f - 1)g\delta^3}}{\sqrt{(\rho^p/\rho^f - 1)gd^3}} \sim \left(\frac{\theta^*}{\phi^{max}\mu_s\left[1 - \tan\alpha/\tan\alpha_0\right]}\right)^{3/2}. \tag{2.23}$$

This approach not only allows us to recover the scaling law of the dimensionless sediment transport rate with the Shields number and the power 3/2 in the high Shields number limit, but also allows to express the influence of the slope through an effective granular friction coefficient $\mu_{eff} = \mu_s\left[1 - \tan\alpha/\tan\alpha_0\right]$. The proposed scaling law is consistent with the original definition of the Shields number as a ratio between the driving and resistive forces applied on the granular phase. Indeed, it represents the ratio between the tangential fluid bed shear stress τ_b and the tangential shear stress associated with the friction between granular layers $\tau = \mu_{eff}P^p = \mu_{eff}(\rho^p - \rho^f)gd$. The dependence of the effective friction coefficient on the distance to the critical debris flow angle, $1 - \tan\alpha/\tan\alpha_0$, is consistent with the analytical analysis of section 2.2, and allows us to take into account both the direct and indirect slope effects on the granular phase in gravity-driven bedload transport. It suggests that the key parameter is not the slope in itself but the ratio between the slope and the critical angle of debris flow. This is of particular importance as the latter is not constant and depends on the maximum solid volume fraction and on the specific density.

3. Numerical Analysis

In order to verify the developed analysis, numerical simulations of turbulent bedload transport are performed using an existing coupled fluid-discrete element model (Maurin *et al.* 2015, 2016).

3.1. *Numerical model*

The model is based on a three-dimensional discrete element method (DEM) coupled with a 1D volume-averaged fluid momentum balance. The fine resolution of the granular phase and the two-way coupling ensures an accurate description of the vertical depth profiles and the momentum conservation of the system on average. The model has been described in details and validated experimentally in Maurin *et al.* (2015), so that only

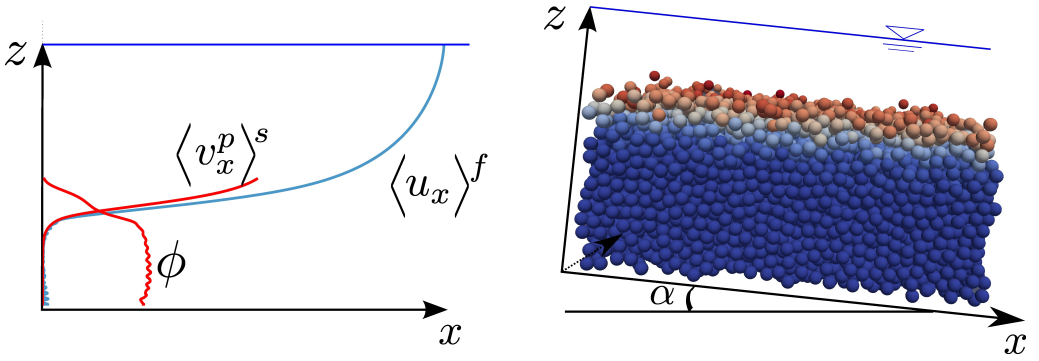

FIGURE 2. Scheme of the numerical setup and its equivalent average unidirectional picture with typical fluid velocity $\langle \mathbf{u}^f \rangle = \langle u_x^f \rangle (z)\ \mathbf{e_x}$, solid volume fraction ϕ, and solid velocity $\langle \mathbf{v}^p \rangle^s = \langle v_x^p \rangle^s (z)\ \mathbf{e_x}$ depth profiles. The inclined 3D bi-periodic granular description is coupled with a unidirectional fluid momentum balance using imposed fixed random bottom boundary condition and water free-surface position. The particle color is representative of the velocity intensity.

the main characteristics are recalled here. The typical configuration considered here is shown in figure 2.

The bi-periodic 3D DEM is based on the explicit resolution of the particle phase, solving the Newton's equations of motion for each particle p at position x_p:

$$m\frac{d^2\mathbf{x}^p}{dt^2} = \sum_{k\in\mathcal{N}} \mathbf{f}_c^{pk} + \mathbf{f}_{ext} = \sum_{k\in\mathcal{N}} \mathbf{f}_c^{pk} + \mathbf{f}_g^p + \mathbf{f}_f^p \tag{3.1}$$

where the sum of the contact forces $\mathbf{f}_c^{pk}$ is made over the ensemble of nearest-neighbours $\mathcal{N}$, $\mathbf{f}_g^p$ is the gravity force, $\mathbf{f}_f^p$ is the force applied by the fluid on particle p. Similarly, the rotation of the particles are solved from the Newton's equations of motion. The contact force between particles is determined from the particles overlap using the classical spring-dashpot contact law (Schwager & Pöschel 2007) which defines a unique normal restitution coefficient e_n, and considers tangential friction characterised by a friction coefficient μ_p. The latter two are taken as respectively $e_n = 0.5$ and $\mu_p = 0.4$, as determined from experimental comparisons (Maurin *et al.* 2015). The interaction with the fluid phase ($\mathbf{f}_f^p$) is restricted to the main contributions, i.e. three dimensional buoyancy ($\mathbf{f}_b^p$) and drag forces ($\mathbf{f}_D^p$) (Jackson 2000; Maurin *et al.* 2015):

$$\mathbf{f}_b^p = -\frac{\pi d^3}{6}\nabla P^f, \tag{3.2}$$

$$\mathbf{f}_D^p = \frac{1}{2}\rho^f \frac{\pi d^2}{4}\, C_D \left|\left|\langle \mathbf{u}\rangle_{\mathbf{x^p}}^f - \mathbf{v^p}\right|\right| \left(\langle \mathbf{u}\rangle_{\mathbf{x^p}}^f - \mathbf{v^p}\right), \tag{3.3}$$

where the average fluid velocity and the fluid pressure are taken at the center of particle p, and $\mathbf{v^p}$ represent the velocity of particle p. The drag coefficient C_D depends on the particle Reynolds number $Re_p = \left|\left|\langle \mathbf{u}\rangle_{\mathbf{x^p}}^f - \mathbf{v^p}\right|\right| d/\nu^f$ and takes into account hindrance effects (DallaValle 1948; Richardson & Zaki 1954): $C_D = (0.4 + 24.4/Re_p)\,(1-\phi)^{-3.1}$. Knowing the position and velocity of the particles, the fluid pressure and velocity fields, the Newton's equations of motion are solved for the ensemble of particles using the open-source DEM code YADE (Šmilauer et al. 2015).

The coupled fluid description solves the volume-averaged momentum balance of the fluid phase, corresponding to equations (2.7) and (2.9):

$$0 = \frac{\partial S_{xz}^f}{\partial z} + \frac{\partial R_{xz}^f}{\partial z} + \rho^f (1-\phi) g \sin\alpha - n \left\langle f_{f\,x}^p \right\rangle^p, \tag{3.4}$$

$$0 = -\frac{\partial P^f}{\partial z} + \rho^f (1-\phi) g \cos\alpha - n \left\langle f_{f\,z}^p \right\rangle^p, \tag{3.5}$$

Due to the steady uniform character of the problem, the fluid velocity field reduces to its streamwise component and depends only on the vertical position: $\langle \mathbf{u} \rangle^f = \langle u_x \rangle^f (z)\ \mathbf{e_x}$, as sketched in figure 2. Therefore, the buoyancy force (eq. 3.2) is restricted to its wall-normal component and equation (3.5) leads to an hydrostatic fluid pressure distribution, the wall-normal average drag force being negligible. The solution of the streamwise fluid phase momentum balance (eq. 3.4) requires closures for the viscous and Reynolds stress tensors, as well as the determination of the solid volume fraction ϕ and the momentum transfer associated with the granular phase interaction. Considering a Newtonian fluid, the viscous shear stress is expressed as:

$$S_{xz}^f = \rho^f (1-\phi) \nu^f \frac{d \langle u_x \rangle^f}{dz}, \tag{3.6}$$

with ν^f the clear fluid kinematic viscosity and $\langle u_x \rangle^f$ the volume-averaged streamwise fluid phase velocity. The Reynolds shear stress is based on the eddy viscosity concept (ν^t) using a mixing length formulation:

$$R_{xz}^f = \rho^f\ \nu^t \frac{d \langle u_x \rangle^f}{dz} \quad \text{with} \quad \nu^t = (1-\phi)\ l_m^2 \left| \frac{d \langle u_x \rangle^f}{dz} \right|, \tag{3.7}$$

where the mixing length is taken similarly to Li & Sawamoto (1995) as:

$$l_m(z) = \kappa \int_0^z \frac{\phi^{max} - \phi(\zeta)}{\phi^{max}}\ d\zeta, \tag{3.8}$$

with $\kappa = 0.41$, the von Karman constant. The formulation adopted allows one to recover the law of the wall (Prandtl 1926) in clear fluid, while completely damping the turbulence inside the granular bed at maximum packing fraction (ϕ^{max}).
The solid volume fraction (ϕ) and the fluid-particle interaction term ($n < f_f^p >^p$) are determined from spatial averaging of the discrete solid phase. Considering cubic boxes of finite wall-normal length scale l_z, these two terms are averaged over the whole length and width of the granular bi-periodic cell. In order to solve the important wall-normal gradients present in turbulent bedload transport, a small wall-normal weighting function length scale has been adopted (typically $l_z = d/30$), and this choice has been validated through the experimental validation (Maurin *et al.* 2015).

The 3D DEM and the fluid model are solved as transient problems applying a fixed bottom boundary condition for both the fluid ($\langle \mathbf{u} \rangle^f (z=0) = 0$) and the particle phase (fixed random particles) and imposing the position of the water free-surface ($d \langle u_x \rangle^f / dz (z = h) = 0$). In order to achieve a stable integration, the DEM time step is bounded by the propagation time of the fastest wave over a particle diameter (Maurin 2015; Maurin *et al.* 2015). The fluid resolution time step corresponds to a typical characteristic evolution time scale of the granular medium and is taken much larger than the DEM one (Maurin *et al.* 2015): $\Delta t_f = 10^{-2} s$ with respect to $\Delta t_p \sim O(10^{-4} - 10^{-5})\ s$. The model has been compared with experiments and has shown its capability to describe

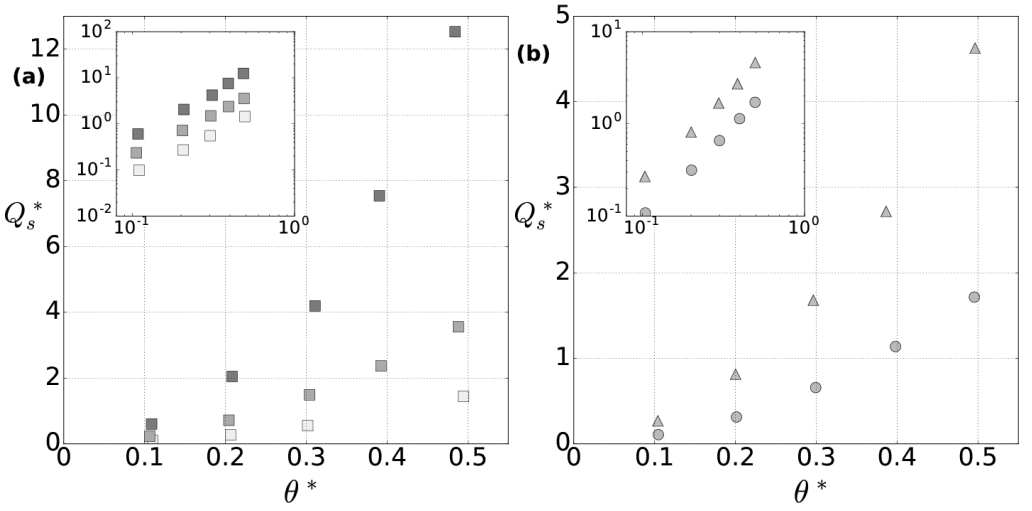

FIGURE 3. Dimensionless sediment transport rate Q_s^* as a function of the Shields number θ^* for variation of slope at a specific density of $\rho^p/\rho^f - 1 = 1.5$ (a) and variation of specific density at a given slope (b) respectively. The triangles, the squares and the circles denote simulations with specific density $\rho^p/\rho^f - 1$ of 0.75, 1.5 and 3 respectively. The darkness of the points is characteristic of the value of the slope angle α varied between 0.02, 0.1, and 0.14 (1, 6 and 9 degrees).

accurately the granular depth structure in turbulent bedload transport (Maurin *et al.* 2015).

3.2. *Results*

In order to study the bulk flow behavior and to investigate the parameter space, bi-periodic three dimensional numerical simulations are performed by varying the Shields number θ^* between the onset of motion θ_c^* and intense bedload transport ($\theta^* \sim 0.6$), the relative slope angle $\tan\alpha/\tan\alpha_0$ between 0.1 and 0.75, and the specific density $\rho^p/\rho^f - 1$ between 0.75 (lightweight plastic), 1.5 (glass/natural sediment) and 3 (metal). In the simulations, the water free-surface position and the channel slope angle are imposed before letting the system evolves under the effect of gravity. After reaching the steady state, the data are processed over a period of $100s$ at $10Hz$, and averaged over time and space (Maurin *et al.* 2015). The Shields number is evaluated by taking the fluid bed shear stress as the maximum of the turbulent Reynolds shear stress.

Figures 3a and 3b show the dimensionless sediment transport rate as a function of the Shields number obtained by varying the channel inclination angle and the specific density respectively. While being far from the threshold of motion, an increase of up to an order of magnitude is observed in the dimensionless sediment transport rate when the slope increases at constant Shields number. This important influence at high Shields number evidences the impact of the slope variation on the sediment transport formula. In addition, the variation of the specific density at constant slope and Shields number is also seen to affect the dimensionless sediment transport rate (see fig. 3b), as expected from the theoretical analysis presented in section 2.

Combining the variation of the slope and of the specific density, figure 4a shows a complex picture of the phenomenon, with an important dispersion at given Shields

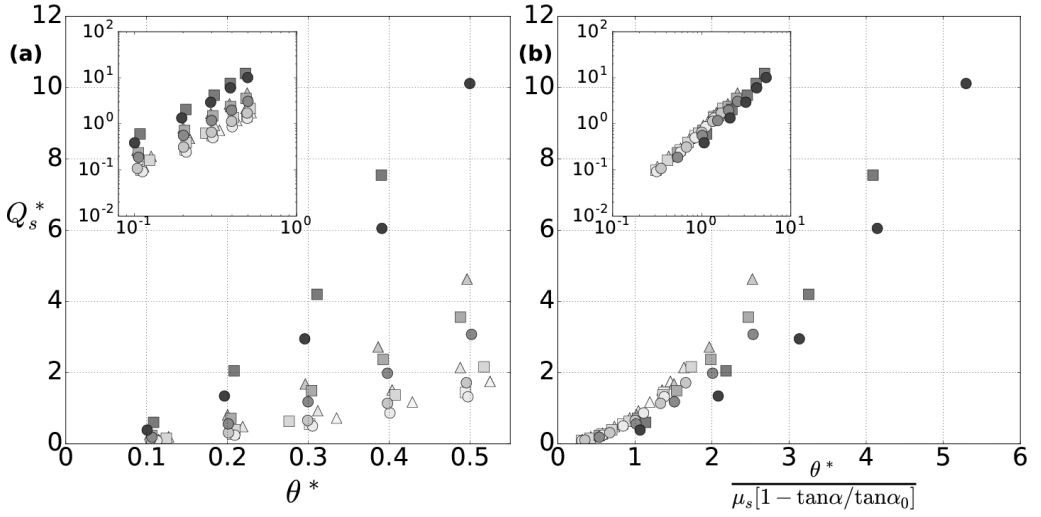

FIGURE 4. Dimensionless sediment transport rate Q_s^* as a function of the Shields number θ^* (a) and the rescaled Shields number (b) respectively, for variation of slope and specific density. The triangles, the squares and the circles denote simulations with specific density $\rho^p/\rho^f - 1$ of 0.75, 1.5 and 3 respectively, and the darkness of the points is characteristic of the value of the slope angle α varied between 0.01 and 0.2 (1 and 12 degrees).

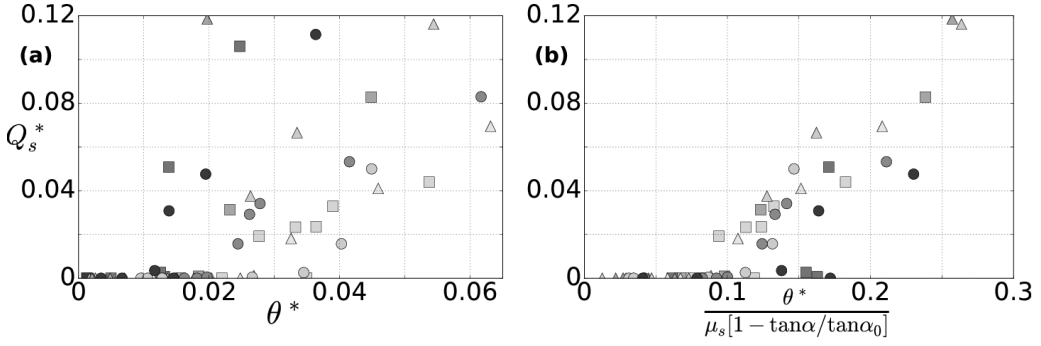

FIGURE 5. Dimensionless sediment transport rate Q_s^* as a function of the Shields number θ^* (a) and the rescaled Shields number (b) respectively, for variation of slope and specific density close to the onset of motion. The color code is the same as the previous figures.

numbers resulting from the coupling between the two mechanisms. Evaluating the granular medium friction coefficient from dry inclined plane avalanche simulations ($\mu_s \simeq 0.4$), the results are plotted in figure 4b as a function of the modified Shields number proposed in the previous section. All the data is shown to collapse on a single curve, with few dispersion at high modified Shields numbers. This collapse shows that the rescaling characterizes at first order the effect of the slope and of the specific density variations on the sediment transport rate in gravity-driven turbulent bedload transport. While the small dispersion observed at high modified Shields numbers highlights the limits of the proposed scaling law, its intuitive nature, its simplicity and the fact that it encompasses the different physical mechanisms represent a clear improvement compared with previous corrections.

Additional simulations have been performed close to the onset of motion to characterize

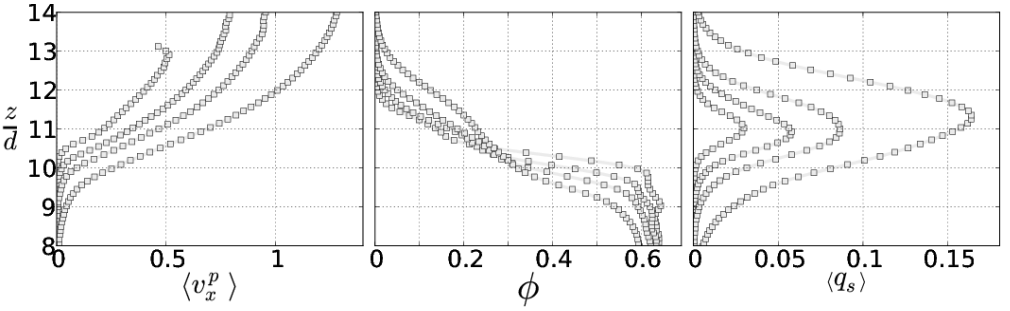

FIGURE 6. Shields number influence on the solid velocity, volume fraction and transport rate density depth profiles, at given slope ($\alpha = 0.02$, 1°) and specific density ($\rho^p/\rho^f = 1.5$). The Shields number is varying between $\theta^* = 0.1$ and $\theta^* = 0.5$.

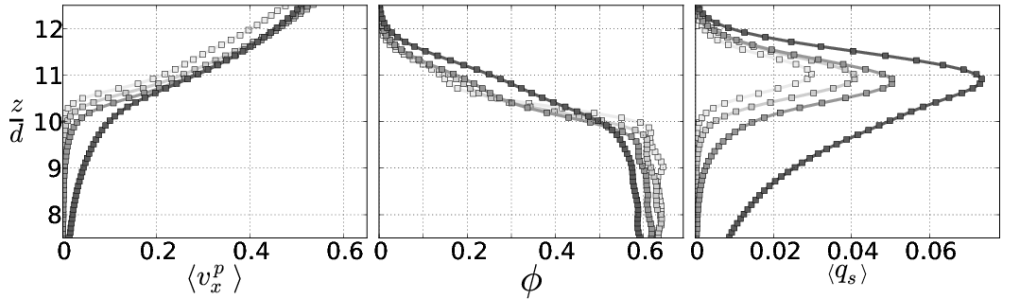

FIGURE 7. Slope influence on the solid velocity, volume fraction and transport rate density depth profiles, at a given Shields number $\theta^* \sim 0.1$ and specific density ($\rho^p/\rho^f = 1.5$). The intensity of the points reflects the magnitude of the slope, which is varying between 1 and 8 degrees ($\alpha \in [0.02, 0.14]$).

the critical Shields number. The latter has been evaluated by forcing the flow slightly above the onset of motion before letting the simulations evolve at the given Shields numbers in order to characterize the cessation threshold. The results are shown in figure 5 and suggest that the proposed rescaling is valid at first order close to the critical Shields number. Even though the data exhibit more dispersion due to the complex characterisation of the onset of motion (Clark *et al.* 2015), the rather good collapse observed suggests that the proposed formulation allows to define a unique critical Shields number independent from the slope and the specific density, which is close to $\theta_c^*/[\mu_s(1 - tan\alpha/\tan\alpha_0)] \simeq 0.1$ in the present simulations.

In order to illustrate the underlying mechanisms of the slope influence on the vertical granular flow structure, the solid depth profiles of volume fraction, ϕ, average streamwise particle velocity, $< v_x^p >$, and transport rate density, $q_s = \phi < v_x^p >$ are shown in figure 6 for various Shields numbers at constant $\tan\alpha/\tan\alpha_0 = 0.1$. The solid volume fraction depth profiles are characterized by the presence of a fixed point at the interface between the granular bed and the fluid flow around $\phi = 0.3$. The Shields number increase leads to an increase of the solid volume fraction above the interface and a decrease below it, associated with an increase of the mobile granular layer thickness. The corresponding solid velocity profiles keep the same shape and exhibit a shift to higher values with increasing Shields numbers, similarly to the transport rate density profiles which are broadening in the same time due to the increased mobile layer thickness.

The presence of the fixed point in the solid volume fraction profiles at a low relative slope inclination angle suggests that an appropriate non-dimensionalization of the z component could collapse all the solid volume fraction profiles obtained at different Shields numbers. However, as we have seen in section 2.2, the vertical structure of the granular flow results from a competition between the slope influence on the lower part of the granular flow and the surface contribution from the dimensionless fluid bed shear stress, i.e. the Shields number. These two effects are mostly independent and they are dominant in the lower part and the upper part of the granular flow respectively. This is well observed when considering the variation of the slope influence ($\tan\alpha/\tan\alpha_0$) at a constant Shields number (see figure 7).

Increasing the slope induces an increasing vertical asymmetry in the transport rate profiles towards the bottom, resulting from a shift of the concentration shoulder to higher solid volume fraction and an increase of the solid velocity in the lower part of the mobile layer. The absence of a fixed point and this changing asymmetry in the solid volume fraction and transport rate density profiles show that the granular depth profiles cannot be self-similar in gravity-driven turbulent bedload transport.

4. Discussion

The present theoretical analysis and numerical simulations of gravity-driven turbulent bedload transport demonstrate that the effect of the slope on the sediment transport rate is not restricted to the critical Shields number, but influence the whole transport rate formula, in agreement with the literature (Smart & Jaeggi 1983; Smart 1984; Rickenmann 1991; Cheng & Chen 2014). It highlights the importance of the critical angle of debris flow in the transport rate prediction. The debris flow angle is representative of the effective resistance of the granular layer at rest and includes both the direct and indirect slope influence on the granular medium. Therefore, the analysis suggests that the key parameter in turbulent bedload transport is not the slope but the ratio between the tangent of the slope angle and the tangent of the critical angle of debris flow, $\tan\alpha/\tan\alpha_0$.

As a consequence, the specific density or density ratio plays a crucial role in the slope effect on the sediment transport rate. A variation of the density ratio has important consequences due to the associated modification of the critical debris flow angle and care should be taken when using model material in experiments. In particular, plastic particles are commonly used for sheet flows and bedload transport experiments (Armanini *et al.* 2005; Larcher *et al.* 2007; Capart & Fraccarollo 2011; Ni & Capart 2015; Revil-Baudard *et al.* 2015), with density of about $\rho^p/\rho^f = 1.2$, leading to a critical debris flow angle divided by four with respect to the classical density ratio for underwater natural sediment, $\rho^p/\rho^f = 2.65$. This modification strongly influences both the sediment transport rate and the vertical structure of the granular flow, preventing a direct application of the results to natural sediment transport. In particular, the absence of concentration shoulder in the solid volume fraction profile measured by Capart & Fraccarollo (2011) and Sumer *et al.* (1996) could be explained by the use of plastic particles in their experiments. Indeed, the resulting higher importance of the fluid contribution inside the granular layer tends to smooth out the concentration shoulder as seen in figure 7.

Lastly, we would like to discuss the common points and differences between the gravity-driven and the pressure-driven configurations in uniform turbulent bedload transport.

To illustrate the comparison, we consider the entrainment mechanisms of the granular medium in the pressure-driven configuration, similarly to section 2.2 for the gravity-driven case. Performing the same integration of the two-phase equation, the shear-to-normal stress ratio in the pressure driven configuration reads (see appendix A):

$$\frac{\tau_{xz}^p(z)}{\tau_{zz}^p(z)} = \frac{\rho^p}{\rho^p - \rho^f}\tan\alpha + \frac{\tau_b}{g\cos\alpha(\rho^p-\rho^f)\bar{\phi}_z(h_p - z)} + \frac{\partial P^f/\partial x}{g\cos\alpha(\rho^p-\rho^f)\bar{\phi}_z}. \quad (4.1)$$

The two first terms on the right hand side correspond to the direct influence of the slope on the granular phase and the Shields number dependence. They are exactly the same as for the gravity-driven case (see equation 2.16). The last term on the right hand side represents the effect of the fluid flow induced by the pressure gradient inside the granular layer and is independent from the slope.

Similarly to the gravity-driven configuration, increasing the slope at a constant Shields number decreases the resistance of the granular bed to entrainment, and one might expect a similar consequence on the transport rate scaling. This suggests that the effect of the slope would not only be restricted to the critical Shields number (Fernandez Luque & Van Beek 1976; Fredsøe & Deigaard 1992; Chiew & Parker 1994; Dey 2003; Andreotti *et al.* 2013), but also affects the whole transport rate formula in pressure-driven bedload transport, as suggested by the experiments of Damgaard *et al.* (1997). In addition, similarly to the gravity-driven case developed in this paper, the importance of the fluid flow inside the granular layer cannot be accounted for in the classical framework in term of Shields number - i.e. dimensionless fluid shear stress at the *top* of the granular bed - and should be considered when modelling pressure-driven bedload transport. This has already been achieved and verified experimentally in laminar bedload transport, and leads to a transport rate scaling law in terms of dimensionless fluid flow rate (Aussillous *et al.* 2013).

Besides, the gravity-driven and pressure-driven configurations do not exhibit the same dependency on the slope. One one hand, the fluid flow inside the granular bed is driven by the slope (eq. 2.16), while on the other hand it is driven by the pressure gradient and independent from the slope (eq. 4.1). As a consequence, the two configurations are different in nature and not equivalent in terms of slope dependency. Therefore, care should be taken to consider configuration where the sub-surface fluid flow contribution is negligible when applying results established for pressure-driven flows (e.g. Chiew & Parker (1994); Dey (2003)) to field prediction and experimental gravity-driven configurations (e.g. Li & Cheng (1999); Wilcock & Crowe (2003); Karmaker & Dutta (2016) among others).

5. Conclusion

Analyzing turbulent bedload transport from a theoretical and numerical point of view, we have clarified the mechanisms and origin of the slope influence and made a step toward a better understanding of the phenomenon. In particular, it has been evidenced that the classical modification of the critical Shields number relies on an expression of the buoyancy force which is not valid for uniform turbulent bedload transport. Focusing on gravity-driven configurations in steady uniform conditions, we have evidenced the entrainment mechanisms of the granular phase and shown the neglected importance of the fluid flow inside the bed. The relative importance of the latter with respect to the surface contribution characterized by the Shields number, affects the vertical structure of the granular flow and the sediment transport rate. The proposed modification of the Shields number to account macroscopically for these mechanisms has been shown to make all the present numerical data collapse onto a single master curve. It evidences

that the key parameter in gravity-driven turbulent bedload transport is not the slope but the ratio between the tangent of the slope angle and the tangent of the critical debris flow angle. The difference is of importance when considering ideal particles for which the density (e.g. plastic) and the shape (e.g. spheres) are different from natural sediments. The proposed framework also allows us to make theoretically the link between bedload transport and debris flow. In addition, the theoretical analysis has evidenced a difference in nature between gravity-driven and pressure-driven configurations with respect to the slope influence. This result underlines the necessity to differentiate the two configurations in the analysis of slope influence on turbulent bedload transport.
The present contribution provides a better understanding of the slope influence in idealized configurations, and represents a step in the understanding and prediction of the slope influence in turbulent bedload transport.

Aknowledgement

We are greatful to Ashley Dudill for English corrections. RM would like to thank Thomas Pähtz, Alain Recking and Laurent Lacaze for fruitful discussions. This research was supported by Irstea (formerly Cemagref), the French national research agency project SegSed ANR-16-CE01-0005, the labex OSUG@2020 and the French Institut National des Sciences de lUnivers program EC2CO-BIOHEFECT and EC2CO-LEFE MODSED.

Appendix A. Pressure-driven vertical granular flow structure

For the pressure-driven case, only the streamwise fluid momentum balance is modified, by replacing the driving slope term with a pressure gradient:

$$0 = \frac{\partial S^f_{xz}}{\partial z} + \frac{\partial R^f_{xz}}{\partial z} - (1-\phi)\frac{\partial P^f}{\partial x} - n\left\langle f^p_{f\,x}\right\rangle^p. \tag{A 1}$$

Contrary to the gravity-driven case, there exists a pressure gradient in the streamwise direction so that the buoyancy force has a streamwise component which can be expressed as $-\phi\frac{\partial P^f}{\partial x}$ and leads to the following reformulation:

$$0 = \frac{\partial S^f_{xz}}{\partial z} + \frac{\partial R^f_{xz}}{\partial z} - \frac{\partial P^f}{\partial x} - n\left\langle f^p_{f\,x}\right\rangle^p. \tag{A 2}$$

Performing the same manipulation of the equations as for the gravity driven case, the shear-to-normal granular stress ratio can be shown to read:

$$\frac{\tau^p_{xz}(z)}{\tau^p_{zz}(z)} = \frac{\rho^f g\sin\alpha\displaystyle\int_z^{h_p}\phi(\zeta)d\zeta}{g\cos\alpha(\rho^p-\rho^f)\displaystyle\int_z^{h_p}\phi(\zeta)d\zeta} + \frac{\tau_b + \frac{\partial P^f}{\partial x}\displaystyle\int_z^{h_p}d\zeta}{g\cos\alpha(\rho^p-\rho^f)\displaystyle\int_z^{h_p}\phi(\zeta)d\zeta}, \tag{A 3}$$

leading to the final equation:

$$\frac{\tau^p_{xz}(z)}{\tau^p_{zz}(z)} = \frac{\rho^p}{\rho^p-\rho^f}\tan\alpha + \frac{\tau_b}{g\cos\alpha(\rho^p-\rho^f)\bar{\phi}_z(h_p-z)} + \frac{\partial P^f/\partial x}{g\cos\alpha(\rho^p-\rho^f)\bar{\phi}_z}. \tag{A 4}$$

REFERENCES

Šmilauer et al. 2015 *Yade Documentation 2nd ed. The Yade Project (http://yade-dem.org/doc/) DOI: 10.5281/zenodo.34073*.

Andreotti, B., Forterre, Y. & Pouliquen, O. 2013 *Granular media: between fluid and solid*. Cambridge University Press.

Armanini, A., Capart, H., Fraccarollo, L. & Larcher, M. 2005 Rheological stratification in experimental free-surface flows of granular-liquid mixtures. *Journal of Fluid Mechanics* **532**, 269–319.

Aussillous, P., Chauchat, J., Pailha, M., Médale, M. & Guazzelli, E. 2013 Investigation of the mobile granular layer in bedload transport by laminar shearing flows. *Journal of Fluid Mechanics* **736**, 594–615.

Bagnold, R. A. 1956 The flow of cohesionless grains in fluids. *Phil Trans R Soc A* **249**, 235–297.

Capart, H. & Fraccarollo, L. 2011 Transport layer structure in intense bed-load. *Geophysical Research Letters* **38** (20), L20402, l20402.

Cheng, N-S. & Chen, X. 2014 Slope correction for calculation of bedload sediment transport rates in steep channels. *Journal of Hydraulic Engineering* **140** (6), 04014018.

Chiew, Y-M. & Parker, G. 1994 Incipient sediment motion on non-horizontal slopes. *Journal of Hydraulic Research* **32** (5), 649–660.

Christensen, B. A. 1995 Incipient sediment motion on non-horizontal slopes. *Journal of Hydraulic Research* **33** (5), 725–730, arXiv: http://dx.doi.org/10.1080/00221689509498569.

Clark, A. H., Shattuck, M. D., Ouellette, N. T. & O'Hern, C. S. 2015 Onset and cessation of motion in hydrodynamically sheared granular beds. *Phys. Rev. E* **92**, 042202.

DallaValle, J. M. 1948 *Micrometrics : The technology of fine particles*, , vol. 2nd edition. Pitman Pub. Corp.

Damgaard, J S., Whitehouse, R J. S. & Soulsby, R L. 1997 Bed-load sediment transport on steep longitudinal slopes. *Journal of Hydraulic Engineering* **123** (12), 1130–1138.

Dey, S. 2003 Threshold of sediment motion on combined transverse and longitudinal sloping beds. *Journal of Hydraulic Research* **41** (4), 405–415.

Duran, O., Andreotti, B. & Claudin, P. 2012 Numerical simulation of turbulent sediment transport, from bed load to saltation. *Physics of Fluids* **24** (10), 103306.

Einstein, HA. 1942 Formulas for the transport of bed sediment. *Transactions of the American Society of Civil Engineers* **107**, 561–574.

Fernandez Luque, R. & Van Beek, R. 1976 Erosion and transport of bed-load sediment. *Journal of Hydraulic Research* **14** (2), 127–144.

Fredsøe, J. & Deigaard, R. 1992 *Mechanics of Coastal Sediment Transport*. World. Scientific.

Frey, P. 2014 Particle velocity and concentration profiles in bedload experiments on a steep slope. *Earth Surface Processes and Landforms* **39** (5), 646–655.

Gilbert, K. G. 1914 *The transportation of débris by running water*. Washinton government printing office.

Hsu, T. J., Jenkins, J. T. & Liu, P. L. F. 2004 On two-phase sediment transport: sheet flow of massive particles. *Proceedings of the Royal Society of London Series A-mathematical Physical and Engineering Sciences* **460** (2048), 2223–2250.

Iversen, J. D. & Rasmussen, K. R. 1994 The effect of surface slope on saltation threshold. *Sedimentology* **41** (4), 721–728.

Iversen, J. D. & Rasmussen, K. R. 1999 The effect of wind speed and bed slope on sand transport. *Sedimentology* **46** (4), 723–731.

Jackson, R. 2000 *The dynamics of fluidized particles*. Cambridge University Press.

Karmaker, T. & Dutta, S. 2016 Prediction of short-term morphological change in large braided river using 2d numerical model. *Journal of Hydraulic Engineering* **142** (10), 04016039.

Larcher, M., Fraccarollo, L., Armanini, A. & Capart, H. 2007 Set of measurement data from flume experiments on steady uniform debris flows. *Journal of Hydraulic Research* **45**, 59–71.

Lhuillier, D. 2011 Personal communication.

Li, F. & Cheng, L. 1999 Numerical model for local scour under offshore pipelines. *Journal of Hydraulic Engineering* **125** (4), 400–406.

Li, L. & Sawamoto, M. 1995 Multi-phase model on sediment transport in sheet-flow regime under oscillatory flow. *Coastal engineering Japan* **38**, 157–178.

Maurin, R. 2015 Investigation of granular behavior in bedload transport using an Eulerian-Lagrangian model. PhD thesis, Université Grenoble Alpes.

Maurin, R., Chauchat, J., Chareyre, B. & Frey, P. 2015 A minimal coupled fluid-discrete element model for bedload transport. *Physics of Fluids* **27** (11), 113302.

Maurin, R., Chauchat, J. & Frey, P. 2016 Dense granular flow rheology in turbulent bedload transport. *Journal of Fluid Mechanics* **804**, 490–512.

Maxey, M. R. & Riley, J. J. 1983 Equation of motion for a small rigid sphere in a nonuniform flow. *Physics of Fluids (1958-1988)* **26** (4), 883–889.

Meyer-Peter, E. & Müller, R. 1948 Formulas for bed-load transport. In *Proc. 2nd Meeting*, pp. 39–64. IAHR.

Ni, W-J. & Capart, H. 2015 Cross-sectional imaging of refractive-index-matched liquid-granular flows. *Experiments in Fluids* **56** (8), 163.

Prandtl, L. 1926 Bericht über neuere Turbulenzforschung. *Hydraulische Probleme. Vorträge Hydrauliktagung Göttingen* **5**, 1–13.

Recking, A., Degoutte, G., Camenen, B. & Frey, P. 2013 *Dynamique et amnagement des torrents et rivires de montagne*, chap. Hydraulique et transport solide, pp. 133–199. Quae.

Revil-Baudard, T. & Chauchat, J. 2013 A two-phase model for sheet flow regime based on dense granular flow rheology. *Journal of Geophysical Research: Oceans* **118** (2), 619–634.

Revil-Baudard, T., Chauchat, J., Hurther, D. & Barraud, P-A. 2015 Investigation of sheet-flow processes based on novel acoustic high-resolution velocity and concentration measurements. *Journal of Fluid Mechanics* **767**, 1–30.

Richardson, J. F. & Zaki, W. N. 1954 Sedimentation and fluidization: Part i. *Trans. Instn. Chem. Engrs* **32**.

Rickenmann, D. 1991 Hyperconcentrated flow and sediment transport at steep slopes. *Journal of Hydraulic Engineering* **117** (11), 1419–1439.

Rickenmann, D. 2001 Comparison of bed load transport in torrents and gravel bed streams. *Water Resources Research* **37** (12), 3295–3305.

Schwager, T. & Pöschel, T. 2007 Coefficient of restitution and linear spring-dashpot model revisited. *Granular Matter* **9**, 465–469.

Shields, A. 1936 Anwendung der Aehnlichkeitsmechanik und der Turbulenzforschung auf die Geschiebebewegung. Doktor-Ingenieurs dissertation, Technischen Hochschule, Berlin.

Smart, G. M. 1984 Sediment transport formula for steep channels. *Journal of Hydraulic Engineering* **110** (3), 267–276.

Smart, G. M. & Jaeggi, M 1983 Sediment transport on steep slopes. *Tech. Rep.* 64. Eth Zurich.

Sumer, B. M., Kozakiewicz, A., Fredsøe, J. & Deigaard, R. 1996 Velocity and concentration profiles in sheet-flow layer of movable bed. *Journal of Hydraulic Engineering* **122** (10), 549–558.

Takahashi, T. 1978 Mechanical characteristics of debris flow. *Journal of the Hydraulics Division* **104** (8), 1153–1169.

Takahashi, T. 2007 *Debris Flow: Mechanics, Prediction and Countermeasures*. Taylor & Francis.

Wilcock, P. R. & Crowe, J. C. 2003 Surface-based transport model for mixed-size sediment. *Journal of Hydraulic Engineering* **129** (2), 120–128.